



Fluorescence imaging of cardiac propagation: spectral properties and filtering of optical action potentials

Sergey F. Mironov, Frederick J. Vetter and Arkady M. Pertsov

Am J Physiol Heart Circ Physiol 291:327-335, 2006. First published Jan 20, 2006;
doi:10.1152/ajpheart.01003.2005

You might find this additional information useful...

This article cites 20 articles, 12 of which you can access free at:

<http://ajpheart.physiology.org/cgi/content/full/291/1/H327#BIBL>

Updated information and services including high-resolution figures, can be found at:

<http://ajpheart.physiology.org/cgi/content/full/291/1/H327>

Additional material and information about *AJP - Heart and Circulatory Physiology* can be found at:

<http://www.the-aps.org/publications/ajpheart>

This information is current as of June 13, 2006 .

AJP - Heart and Circulatory Physiology publishes original investigations on the physiology of the heart, blood vessels, and lymphatics, including experimental and theoretical studies of cardiovascular function at all levels of organization ranging from the intact animal to the cellular, subcellular, and molecular levels. It is published 12 times a year (monthly) by the American Physiological Society, 9650 Rockville Pike, Bethesda MD 20814-3991. Copyright © 2005 by the American Physiological Society. ISSN: 0363-6135, ESN: 1522-1539. Visit our website at <http://www.the-aps.org/>.



Fluorescence imaging of cardiac propagation: spectral properties and filtering of optical action potentials

Sergey F. Mironov,^{1,*} Frederick J. Vetter,^{2,*} and Arkady M. Pertsov¹

¹Department of Pharmacology, State University of New York, Upstate Medical University, Syracuse, New York; and ²Biomedical Engineering Program, Department of Electrical and Computer Engineering, University of Rhode Island, Kingston, Rhode Island

Submitted 19 September 2005; accepted in final form 17 January 2006

Mironov, Sergey F., Frederick J. Vetter, and Arkady M. Pertsov. Fluorescence imaging of cardiac propagation: spectral properties and filtering of optical action potentials. *Am J Physiol Heart Circ Physiol* 291: H327–H335, 2006. First published January 20, 2006; doi:10.1152/ajpheart.01003.2005.—Fluorescence imaging using voltage-sensitive dyes is an important tool for studying electrical propagation in the heart. Yet, the low amplitude of the voltage-sensitive component in the fluorescence signal and high acquisition rates dictated by the rapid propagation of the excitation wave front make it difficult to achieve recordings with high signal-to-noise ratios. Although spatially and temporally filtering the acquired signals has become de facto one of the key elements of optical mapping, there is no consensus regarding their use. Here we characterize the spatiotemporal spectra of optically recorded action potentials and determine the distortion produced by conical filters of different sizes. On the basis of these findings, we formulate the criteria for rational selection of filter characteristics. We studied the evolution of the spatial spectra of the propagating wave front after epicardial point stimulation of the isolated, perfused right ventricular free wall of the pig heart stained with di-4-ANEPPS. We found that short-wavelength (<3 mm) spectral components represent primarily noise and surface features of the preparation (coronary vessels, fat, and connective tissue). The time domain of the optical action potential spectrum also lacks high-frequency components (>100 Hz). Both findings are consistent with the reported effect of intrinsic blurring caused by light scattering inside the myocardial wall. The absence of high-frequency spectral components allows the use of aggressive low-pass spatial and temporal filters without affecting the optical action potential morphology. We show examples where the signal-to-noise ratio increased up to 150 with <3% distortion. A generalization of our approach to the rational filter selection in various applications is discussed.

voltage-sensitive dyes; spatial spectrum analysis; cardiac electrophysiology; linear low-pass filtering

FLUORESCENCE IMAGING using voltage-sensitive dyes has become a major tool for studying electrical activation in the heart. Yet, because of the low amplitude of voltage-sensitive component of the signal [usually not more than 10% of total fluorescence (4)] and rapid propagation of excitation wave in the heart (~0.5 m/s), recording optical action potentials (OAPs) remains a significant technological challenge, requiring high acquisition speeds and transducers with a very wide dynamic range. Contemporary CCD cameras, CMOS cameras, and photodiode arrays used in optical mapping of cardiac propagation run up to 10,000 frames/s. At such acquisition rates, it is extremely difficult to achieve high signal-to-noise ratios, which makes

spatial and temporal filtering of the acquired signals one of the key elements of optical mapping.

Although spatial and temporal filtering is routinely used in optical mapping studies, there is no consensus regarding the design and use of such filters. There is a concern that filtering decreases spatial resolution and induces distortion. Thus some researchers avoid applying any spatial filters (2), whereas others use complicated adaptive filters (14, 21, 22). This indicates a great need for the development of quantitative criteria that would enable a rational design strategy for spatial and temporal filters in a given application.

The goals of this study were to assess the spatial and temporal spectral characteristics of optically recorded action potentials, design an experimental procedure for selecting the optimal linear filter characteristics, and determine the level of distortions produced by the resulting filters. It is well known that aggressive filtering reduces the noise. The main question, however, is how much filtering can be afforded without significantly distorting the signal? The answer to this question can be obtained only by looking at how the given filtering procedure affects the signal itself. To approximate the uncorrupted signal as closely as possible, we select recordings with better signal-to-noise ratios and subsequently use ensemble averaging. After the spectral characteristics of the pure signal are determined and appropriate filter characteristics (as broad as possible, yet not causing significant signal distortion) are chosen, the filters are applied to raw signals, and their effect is evaluated.

We demonstrate that in three-dimensional pig ventricular wall preparations, spatial filters with kernel diameter as large as 3 mm produce <4% distortion. Temporal filters with five-frame kernels can also be safely used in such preparations even at modest acquisition rates (with 800-frames/s movies). We show examples where applying such filters to raw data significantly increased the signal-to-noise ratio in both the space and time domains. Combining both spatial and temporal filters can improve the signal-to-noise ratio by an order of magnitude and is comparable to ensemble averaging of 100 optical action potentials. The application and limitations of our approach for selecting the parameters of spatial and temporal filters in various optical mapping settings are discussed.

METHODS

Experimental preparation. All experimental protocols conformed to the *Guide for the Care and Use of Laboratory Animals* (NIH Publication no. 85–23, Revised 1996) and were approved by the State

* S. F. Mironov and F. J. Vetter contributed equally to this work.

Address for reprint requests and other correspondence: A. M. Pertsov, Dept. of Pharmacology, SUNY Upstate Medical Univ., 750 East Adams St., Syracuse, NY 13210 (e-mail: pertsova@upstate.edu).

The costs of publication of this article were defrayed in part by the payment of page charges. The article must therefore be hereby marked “advertisement” in accordance with 18 U.S.C. Section 1734 solely to indicate this fact.

University of New York Upstate Medical University Institutional Animal Care and Use Committee. Young pigs ($n = 11$) were heparinized (500 IU iv) and subsequently anesthetized with pentobarbital sodium (35 mg/kg iv). The heart was rapidly removed and Langendorff (retrograde) perfused with cold (4°C) cardioplegic solution (10). The right ventricular free wall was quickly excised, and one of the large coronary arteries was cannulated. Nonperfused tissue was removed, and the preparation was mounted in a transparent frame as described in Zaitsev et al. (23).

Preparations were perfused with a standard oxygenated Tyrode solution (2, 20) at 80 mmHg and superfused with the same solution at a rate of 40 ml/min. Diacetyl monoxime was added to the Tyrode solution (15 mmol/l) to suppress contractions and eliminate motion artifacts. The voltage-sensitive dye di-4-ANEPPS (15 μ g/ml) was added to the perfusate as described previously (9). The preparation was paced at a point on the epicardial surface with a basic cycle length of 500 ms at twice diastolic threshold.

Optical mapping. Movies were acquired using a high frame-rate 12-bit digital CCD camera (Dalsa CA-D1-0128T) in 2×2 binning mode for a final resolution of 64×64 pixels. The camera was fitted with a Computar lens (relative aperture 1:1.2, 12-mm focal length) that provided an object field of view of $\sim 25 \times 25$ mm. The movies were acquired at 800 frames/s. Ensemble averaging at each pixel was performed over 100 or more propagating wave fronts synchronized with stimuli markers recorded during acquisition. For spatial and temporal filtering the weighting coefficient, $w(i, j)$, was computed using a triangular (Bartlett) window function (17). The weighting coefficient was maximal at the central pixel (Eq. 1) and linearly decreased toward the edge of the kernel

$$w(i, j) = 1 - \sqrt{\frac{k^2 + l^2}{m^2}} \text{ for } k^2 + l^2 < m^2, 0 \text{ otherwise} \quad (1)$$

where m is the kernel size in pixels and $-m/2 < k, l < m/2$.

Spatial filtering was carried out with conical filters using kernels ranging from 3×3 to 25×25 pixels. Temporal filtering was performed similarly as weighted averages over a sequence of three or five frames with maximal weight on the central frame.

Noise measurement. In the time domain, the signal-to-noise ratio was calculated as ratio of signal amplitude for each pixel (calculated after ensemble averaging) to the root-mean-square (RMS) of each pixel in the image obtained during a diastolic interval recording. The RMS was calculated as

$$\text{RMS} = \sqrt{\frac{\sum_i (f_i - \bar{f}_i)^2}{n}} \quad (2)$$

where f_i is the intensity of the pixel in the i th frame after the stimulus, \bar{f}_i is averaged intensity for nine neighbor (from $i - 4$ to $i + 4$) frames, and n is number of frames in the ensemble.

Distortion measurement. Signal distortion for each pixel was calculated as the ratio of the square root of the mean deviation of the filtered movie from the ensemble-averaged (EA) movie to the signal amplitude calculated from the EA movie:

$$d_{x,y} = \frac{1}{N} \sqrt{\frac{\sum_N (F_{x,y}^{\text{exp}} - F_{x,y}^{\text{EA}})^2}{F_{x,y}^{\text{max}} - F_{x,y}^{\text{min}}}} \quad (3)$$

where $F_{x,y}^{\text{exp}}$ and $F_{x,y}^{\text{EA}}$ are the pixel values in the filtered and EA movie, respectively; N is the number of frames in the movie; and $F_{x,y}^{\text{max}}$ and $F_{x,y}^{\text{min}}$ are the maximal and minimal values of the pixel, respectively, in the EA movie over the N frames. The distortion d for the entire movie was calculated by averaging the pixel $d_{x,y}$ values.

Frequency spectra. To obtain the spatial spectra, we applied a two-dimensional (2-D) fast Fourier transform (FFT) to each frame of the movie. The 2-D Fourier transform was computed by first trans-

forming each row in the image, replacing each row with its transform, and then transforming each column, replacing each column with its transform (19). We rearranged the quadrants of the resulting spectrum to place the zero frequency component at the center of the spectral image. Spectra were normalized to the noise level in the raw signal. Because the range of the power values in the spectra is very wide, for imaging purposes all spectra were limited by a level of 5.0 (arbitrary units).

To analyze the spatial frequencies, we rotationally averaged the spatial spectra (1, 7). The values of the spatial power spectrum were averaged over all pixels at a given radius from the center of the spatial spectrum.

To obtain the averaged temporal spectra, we calculated the individual spectrum for each pixel in every frame of the movie. Finally, the individual pixel spectra were averaged to obtain a single temporal spectrum for the entire movie.

RESULTS

Ensemble averaging. To generate standard data sets that could be used for analysis of spectral characteristics of OAPs and for assessing the distortions caused by filtering procedures, we used ensemble averaging of the raw data. Figure 1A shows a sequence of normalized frames from an EA movie of wave propagation. In the later frames the shadow of unipolar stimulus electrode is visible, extending from the top left to the center of the preparation. Wave fronts had an elongated elliptical shape (anisotropic ratio of 1.4). Epicardial features such as coronary vessels and fatty tissue became visible as the wave front propagated on the surface of the specimen. Relative to the raw movie, this ensemble average of 124 OAPs improved the signal-to-noise ratio from 12.6 to 125.8 (Table 1), resulting in a movie of sufficient quality to serve as a reference data set.

Spatial spectra. The EA movie in Fig. 1A shows an expanding excitation wave produced by point stimulation of the epicardial surface. The spatial spectra of the respective individual snapshots are shown in Fig. 1B. The lowest spatial frequencies, which correspond to the largest image features, are located in the center of each spectrum, and high spatial frequencies appear at the periphery. All spectra have a dense, bright core surrounded by a diffuse cloud of gray pixels. Spectra of the later phases of propagation show well-defined diagonal and vertical bands. As time increased and the wave front spread across the field of view, the high-frequency content diminished in the images; the vertical and horizontal bands visible during the late phases of propagation were an effect of the propagating wave front reaching the horizontal and vertical boundaries, respectively, of the field of view.

To determine the origin of specific spectral components and the significance of the diagonal bands, we selectively eliminated the respective components and evaluated the effect on the image by applying an inverse FFT. Figure 2A, *top*, shows a snapshot of the wave front (frame 9 from Fig. 1A), which occupies approximately half the field of view. Figure 2A, *bottom*, shows the corresponding spatial power spectrum. The spectrum consists of three main components: the dense core at the center, a diffuse cloud of gray pixels around the core, and a diagonal band. The diagonal band in the spectrum was caused by the shadow of the stimulating electrode in the snapshot (arrow in Fig. 2A) because the orientation of the band is orthogonal to the direction of the electrode shadow. This was demonstrated by eliminating the diagonal band with a notch filter (Fig. 2B, *bottom*) and applying the inverse FFT; the

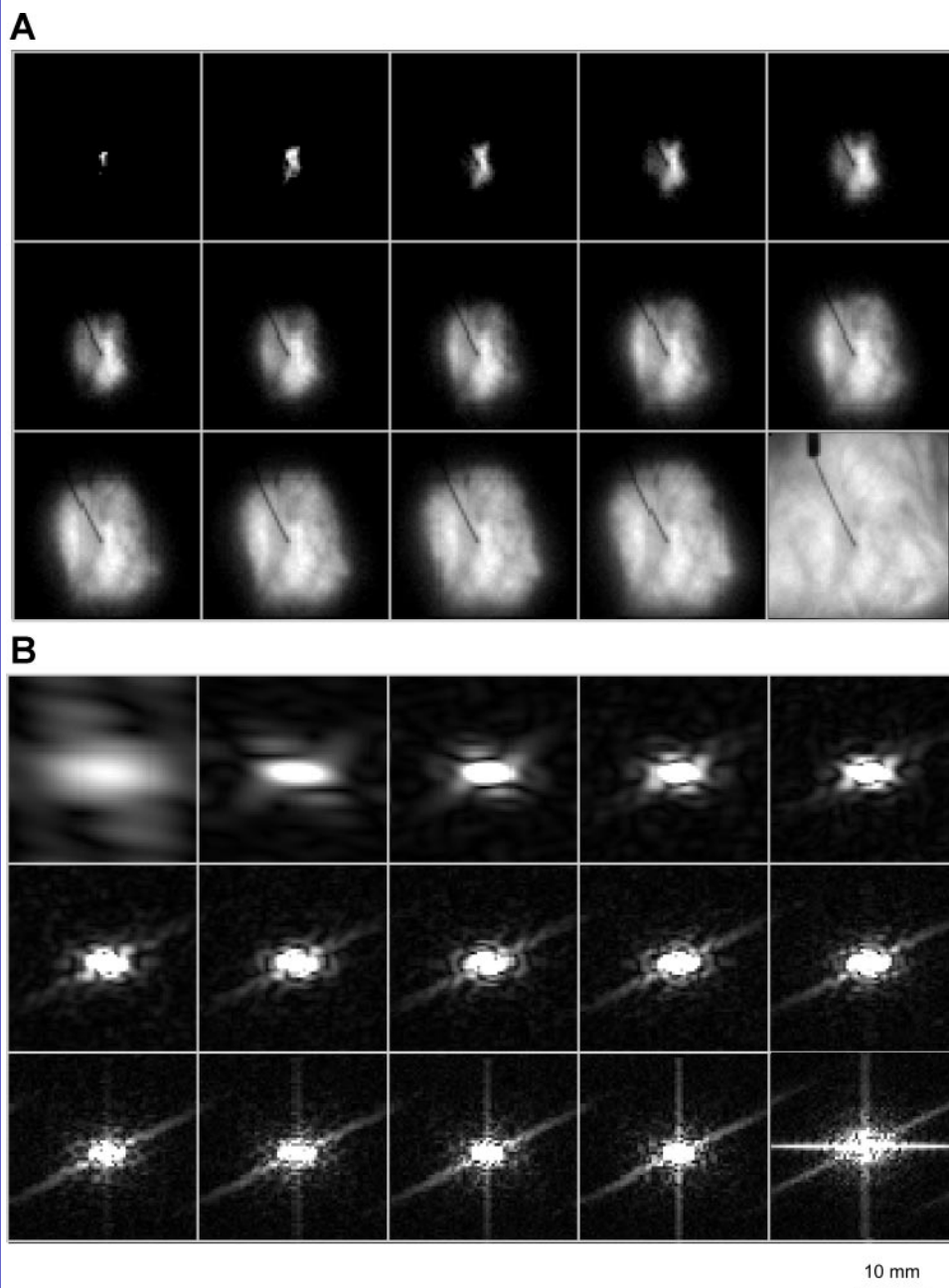


Fig. 1. *A*: sequential snapshots of wave front propagation after point stimulation. Time interval between snapshots was 1.25 ms. *B*: spatial power spectra of each snapshot shown in *A*, computed by using a 2-dimensional fast Fourier transform (FFT). Note the emergence of the vertical band in the spectra as the wave front reaches the lower image boundary. This effect is strongest in the last frame (captured at 35 ms), where the wave front is sharply truncated by the vertical boundaries, causing the strong horizontal band in the spectrum.

electrode shadow was removed from the time domain image (Fig. 2*B*, top). Removing the dense spectral core (Fig. 2*C*) resulted in subtracting the propagating wave front, leaving only small (high frequency) features in the time domain image.

Table 1. *S/N* (Eq. 2) and *distortion* (Eq. 3) of the raw and filtered movies relative to the ensemble-averaged movie

Movie Type	S/N	Distortion, <i>d</i>
Raw image	12.6	7.3
Ensemble averaged	125.8	0
7 × 7 Pixel kernel	71.6	2.9
13 × 13 Pixel kernel	100.7	3.4
7 × 7 Pixel kernel and 5-frame kernel	144.3	3.1

S/N, signal-to-noise ratio.

Finally, removing the diffuse cloud resulted in a smooth and clear image of the propagating wave front (Fig. 2*D*). This suggests spectral components pertinent to wave propagation are concentrated in the low-frequency core of the spectrum.

Elucidating the role of specific spectral components in Fig. 2 provides a key to understanding the time evolution of the spatial spectra illustrated in Fig. 1*B*. The spatial spectra in Fig. 1*B* reflect two different processes: the spatial expansion of the wave front itself (manifested by the shrinkage of the dense spectral core), and the appearance of multiple small anatomic features that became visible when reached by the wave front (the diffuse cloud of pixels around the core). Indeed, as the wave front expands, the number of visible anatomical features increases, which increases the intensity of the diffuse cloud around the core in the spatial spectra. The same effect causes

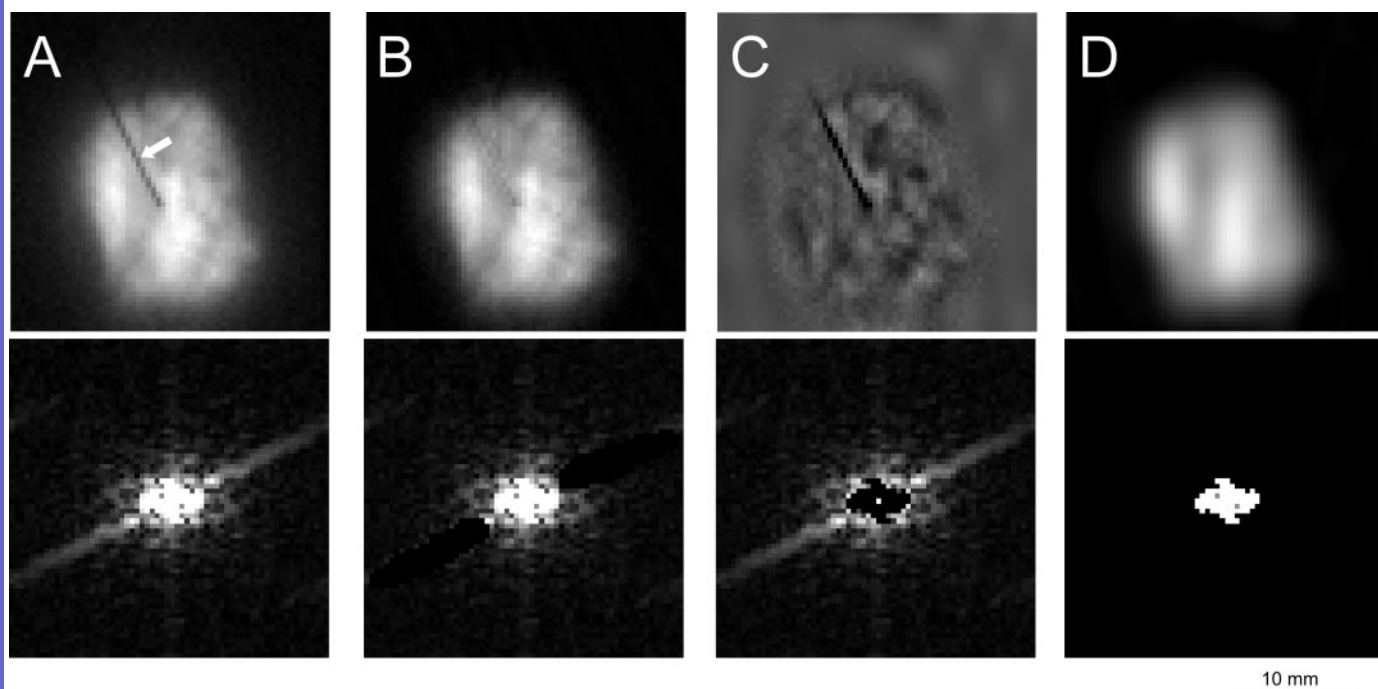


Fig. 2. Components of the spatial power spectrum. *Top* row shows the images of the wave front (*frame 9* in Fig. 1A); *bottom* row shows the spatial power spectrum. *A*: original time domain image (*top*) and corresponding spatial spectrum. Arrow indicates the shadow of the stimulus electrode. *B*: time domain image (*top*) generated by the inverse FFT of the power spectrum (*bottom*) after removing the diagonal band with a notch filter. *C*: image generated by the inverse FFT (*top*) after removing the low-frequency core from the spatial spectrum (*bottom*). *D*: image generated by the inverse FFT (*top*) after removing the high-frequency components from the power spectrum (*bottom*).

the increase of intensity of the diagonal band (compare Fig. 1B, *top* and *middle* rows) corresponding to the stimulating electrode (see Fig. 2B).

To quantify the time evolution of the spatial spectra, we constructed the plot shown in Fig. 3, which is a horizontal stack of 50 sequential rotationally averaged spatial spectra. This plot eliminates the anisotropy of propagation, thus allowing us to identify the major phases in the evolution of the spectrum over

time. Columns in the plot represent the averaged spectra for all pixels equidistant from the center, thus having the same spatial frequency. The plot shows that the high-frequency components due to the propagating wave front constitute the early spectra, but these components diminish during the first 16 ms as the wave front expands over the field of view. In later images, the high-frequency components return when the stimulus electrode, boundary effects, and small surface features of the specimen dominate the image.

The leftmost column in the plot of Fig. 3 represents the spectrum of the first image (see *inset* below the column). The nonzero portion of this column extends down from the longest wavelength (64 pixels) to ~5 pixels, indicating that the image contained substantial high-frequency components. As time increased and the wave front spread across the field of view, the high-frequency content diminished in the images; this is consistent with the individual spectra in the second row of Fig. 1B and the progressive shortening of the nonzero portions of the columns in the plot of Fig. 3. The reduction of high frequencies continued until 16 ms (Fig. 3, second dashed line and *inset*). After this, the intensity of the high frequencies increased again (see second row of spectra in Fig. 1B) and reaches maximum after ~31 ms. At this time, the wave occupies the entire field of view (Fig. 3, *right* dashed line), and this late image contains only a small portion of the wave front (Fig. 3, *right inset*). The spectra of these late-phase images contain a very high level of the high frequencies due to boundary effects and small surface features as explained above.

Spatial filtering. On the basis of the plot of Fig. 3, we chose two different strategies for spatial filtering. The first was a conservative strategy to maximally preserve the useful signal.

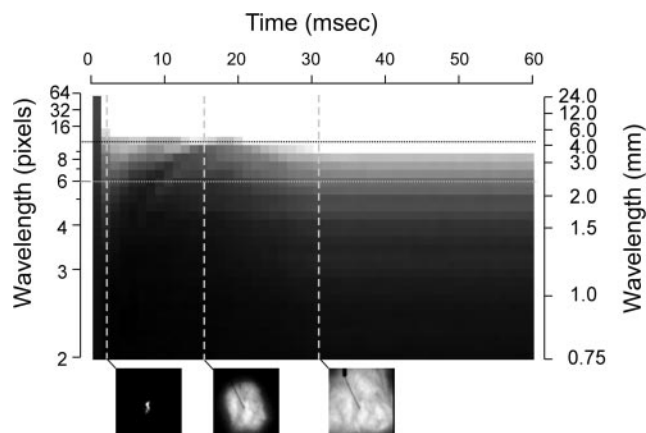


Fig. 3. Time evolution of the spatial spectrum. The main panel shows a stack of the rotationally averaged spectrum from 50 frames. *Insets*: images along the bottom show frames of the propagating wave front in the time domain. The nonzero portion of the leftmost column extends from a wavelength of 64 pixels down to 6 pixels. In subsequent columns (up to 16 ms, middle dashed line), the nonzero portion progressively shortens, indicating less high-frequency content in the images. After 16 ms, the high-frequency content gradually returns, lengthening the nonzero portions of the columns. Beyond 31 ms (*right* dashed line), the spectra are uniform.

The kernel size was determined by the length of the nonzero portion in the earliest spectrum (the horizontal white dotted line in Fig. 3) and equaled 6 pixels. However, because the conical spatial filter used the peripheral pixels with minimal weight and, respectively, should have smaller effective size, we chose a kernel that was one pixel wider, or 7×7 pixels (2.8×2.8 mm). The second strategy was more aggressive and was based on the narrowest spectrum (horizontal black dotted line). We chose the second filter with a kernel size of 13×13 pixels (5.2×5.2 mm) to preserve the wave front shape only during the late phases of propagation, with any distortion concentrated in the earlier phases.

Results of applying these filters are shown in Fig. 4. Figure 4A shows a snapshot of the raw movie (top image) and its spatial spectrum (bottom image) before application of the filters. Figure 4B shows the same snapshot from the EA movie, and the corresponding spectrum. The spectra of spatially filtered images, shown in Fig. 4, C and D, are similar to the spectrum of the EA image in that all have the same dense core, but the vertical and diagonal bands emanating from the core were markedly weakened by spatial filtering.

Applying the conservative 7×7 pixel filter kernel (Fig. 4C) eliminated the noise and extrinsic elements of the image but preserved the overall contour of the wave front. The shadow of the stimulus electrode was still visible (Fig. 4C, black arrow in top image). The 13×13 pixel kernel completely eliminated the shadow of the electrode (Fig. 4D) and somewhat blurred the wave front; the overall contour of the front, however, was not significantly affected. Figure 4E compares the isochronal maps showing sequential positions of the expanding wave fronts derived from the EA (black lines), 7×7 pixel (dotted), and 13×13 pixel (gray) filtered movies. The isochrones follow each other very closely; phase differences usually did not exceed one frame (1.25 ms).

Spatial filtering not only improved the images by eliminating spatial noise and extrinsic detail but also significantly improved the signal-to-noise ratio in the time domain. The effect

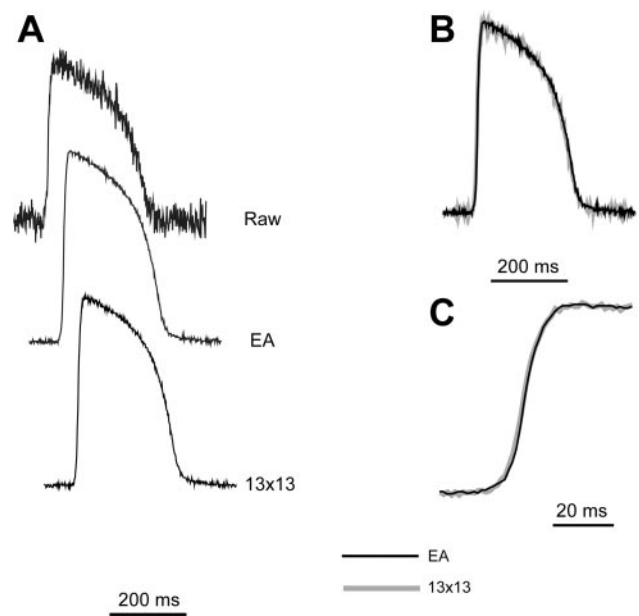


Fig. 5. Effects of spatial filtering on the time domain image. A: optical action potentials from one pixel in the raw movie (top), the ensemble-averaged movie (middle), and the movie after filtering with the 13×13 pixel kernel (bottom). The filtered optically recorded action potentials are shifted only for visualization; the filtering operations did not induce the delay. B: superimposed optical action potentials from the ensemble-averaged movie (black) and the 13×13 pixel kernel filtered movie (gray). C: magnified optical upstrokes from B show no distortion after spatial filtering.

of spatial filtering on the OAP signal is shown in Fig. 5. Figure 5A shows OAPs obtained from a single pixel of the raw movie (top trace), of the EA movie (middle trace), and after applying the 13×13 pixel kernel to the raw movie (bottom trace). Spatial filtering significantly decreased the noise, and the shape of the filtered OAP closely resembles the shape of the EA OAP. For a more detailed comparison, we superimposed OAP

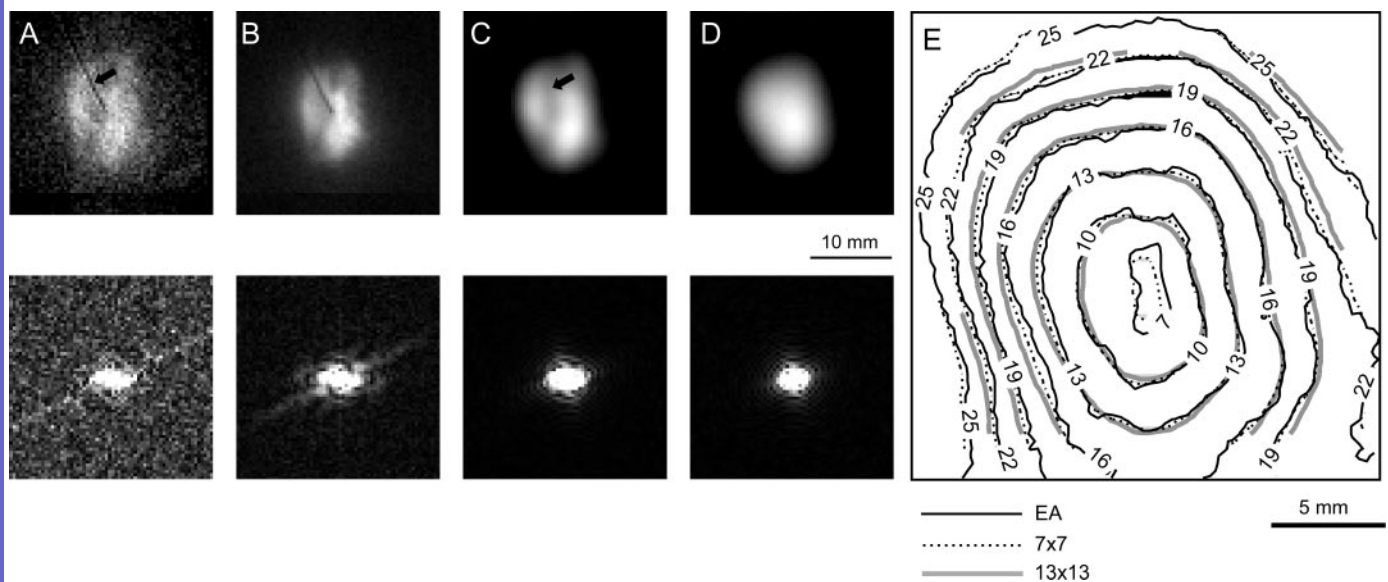


Fig. 4. Spatial filtering of a wave front snapshot (frame 7 from Fig. 1A). Top row shows the raw and filtered time domain images. Bottom row shows the spatial power spectra (power < 1.0). A: raw image. B: image after ensemble averaging with 120 frames. C: raw image filtered with the 7×7 pixel kernel. D: raw image filtered with the 13×13 pixel kernel. E: isochronal maps, calculated at 50% of maximum amplitude, obtained from the ensemble-averaged (EA) movie (solid black lines) and from movies after spatial filtering with a 7×7 pixel kernel (dotted lines) or a 13×13 pixel kernel (gray lines).

upstrokes from the EA and 13×13 kernel filtered movies (Fig. 5B); there was excellent agreement between both OAP traces. Figure 5C shows superimposed OAP upstrokes from the EA movie (black line) and the 13×13 pixel filtered movie (gray line). The upstroke from the filtered movie is nearly identical to the one obtained from the EA movie.

To quantify the distortion induced by the spatial filters, we calculated the root mean square deviation of the filtered movie relative to the EA movie (see METHODS). Figure 6 shows the signal-to-noise ratio and distortion calculated for spatial filter kernel sizes ranging from 3×3 (1.2×1.2 mm) to 25×25 (10×10 mm) pixels. The signal-to-noise ratio (Fig. 6A) rapidly increased with kernel sizes up to 11×11 pixels (4.4×4.4 mm), but the improvement was less dramatic for larger kernels. The dependence of the distortion on kernel size was nonmonotonic (see Fig. 6B): initially the distortion rapidly decreased, then slowly increased, with larger kernel sizes.

The nonmonotonic dependence has the following explanation. The distortion has two different sources. One source of distortion is the noise, which is maximal in the raw movie and still present in the EA movie (Fig. 4, A and B). Expanding the kernel size effectively decreased the noise-related distortion. The distortion never reached zero because the EA movie was not an ideal signal (it still contains noise). The second source of distortion is the attenuation of the components of the OAP signal. Kernels larger than 7×7 pixels (2.8×2.8 mm) progressively remove more of the OAP signal, increasing the distortion. The high frequencies in the OAP signal are attenuated first by kernels immediately above the 7×7 pixel threshold. Expanding the kernel more lowers the cut-off frequency of the filter, leaving only the low-frequency content of the original OAP signal. This effect is apparent in the snapshots of Fig. 4D, where the leading edge of the wave front is blurred compared with the wave front filtered with the 7×7 pixel kernel (Fig. 4C). Distortion for kernels larger than 7×7 pixels was nearly linear and resulted only in changing the OAP amplitude (compare Fig. 5, B and C).

Temporal spectra and filtering. Figure 7A shows normalized power spectra achieved by averaging the individual temporal spectra computed from each pixel in the movie. The dashed line in Fig. 7A shows the temporal spectrum of the raw movie. The temporal spectrum had a flat portion caused by noise at frequencies above 100 Hz. The small peak near 120 Hz is likely a harmonic of 60 Hz power line interference. Spatial

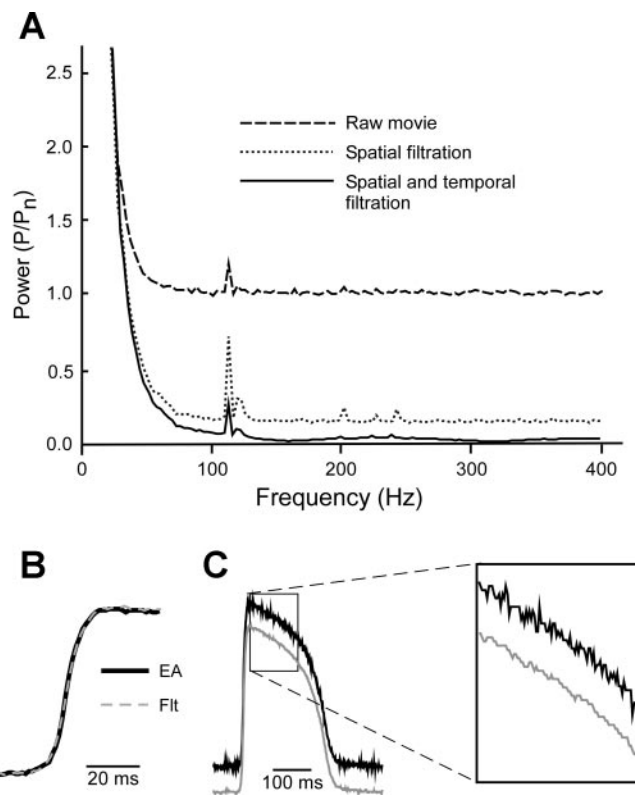
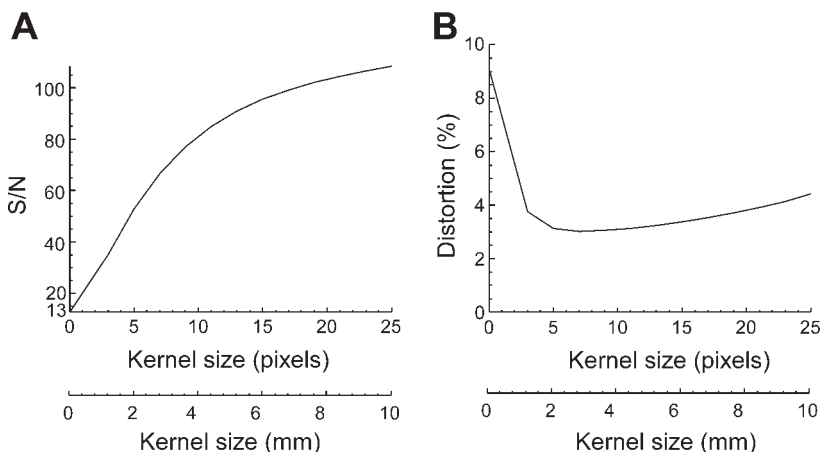


Fig. 7. Effects of combined spatial and temporal filtering on the power spectrum and optical action potential morphology. A: average time spectral power of the raw movie (dashed line), after filtering with the 7×7 pixel kernel (dotted line) and after filtering with the 7×7 pixel kernel followed by 5-frame temporal filtering (solid line). Note the significant reduction in noise power above 80 Hz for the combined spatial-temporal filtered signal. B: superimposed optical action potential upstrokes from the ensemble-averaged movie (black line) and the spatial-temporal filtered movie (dashed gray line). C: high-frequency noise is suppressed in the spatial-temporal filtered optical action potential (gray line) vs. the ensemble-averaged signal (black line).

filtering with the 7×7 pixel kernel (2.8×2.8 mm) significantly decreased the noise power (Fig. 7A, dotted line), but none of the spatial filters removed all the noise. The residual noise had low spatial frequency and power above 100 Hz in the temporal spectrum. This residual noise power originated partially from the light source (peak at 120 Hz) because fluctua-

Fig. 6. Changes in signal-to-noise ratio (S/N) and distortion relative to the ensemble-averaged movie with different spatial filter kernels. A: signal-to-noise ratio as a function of kernel size. B: difference between the spatially filtered movies and the ensemble-averaged movie relative to average signal amplitude as computed with Eq. 3.



tions in the illumination were synchronous for the entire image and cannot be removed by any spatial filter.

To eliminate synchronous noise after spatial filtering, we applied an additional temporal filter. This filter was sized according to the temporal spectra; in this case the useful signal (the low-frequency exponential portion of the spatially filtered movie) ranged from approximately 0 to 120 Hz. Thus, for a sampling rate of 800 frames/s, the temporal filter kernel should not exceed 6 frames to preserve the frequencies below 133 Hz. Applying a 5-frame temporal filter significantly decreased the high-frequency noise (solid line in Fig. 7A). Superimposed OAP upstrokes are nearly indistinguishable between the EA and spatial-temporal movies (Fig. 7B), but high-frequency noise was significantly reduced in the spatial-temporal filtered signal (Fig. 7C and *inset* and Table 1).

Figure 8A shows the effect of varying the additional temporal filter kernel size after applying various spatial filters. Even minimal temporal filtering (3-frame kernel, Fig. 8A, *middle* trace) significantly increased the signal-to-noise ratio. Figure 8B shows that distortion was not significant relative to the EA movie. Thus additional temporal filtering after spatial filtering significantly decreased noise but did not induce additional distortion (Fig. 7C).

DISCUSSION

One of our main findings is that in thick ventricular preparations, short-wavelength components (<3 mm) of the spectra represent primarily noise and surface features (coronary vessels, fat, and connective tissue) of the preparation. Eliminating these components using classical low-pass spatial filters enabled us significantly to improve the quality of the images without affecting the shape of the excitation front. Spatial filtering not only improved quality of optical images but also significantly increased the signal-to-noise ratio in the time domain. Kernels of 13×13 pixels increased the signal-to-noise ratio of OAPs from 12.6 in raw recordings to 100.7 after spatial filtering (Table 1), comparable to movies obtained by ensemble averaging of 100 or more recordings.

Our analysis of temporal spectra revealed that the OAP also lacks high-frequency components above 100 Hz. This should allow the use of small (3-frame) temporal kernels even at modest acquisition rates of 400 frames/s. At 2,000 frames/s, temporal low-pass filters with kernels as large as 15 frames could be used without significantly distorting the optical signal.

Because the filters we used are linear, they can be applied sequentially in either order. Spatial filtering removes asynchronous noise produced by the recording device (i.e., noise uncorrelated with the timing of image acquisition), while temporal filtering removes synchronous noise produced by the light source; this noise is uniform within a single image but varies across images due to fluctuations in the illumination. Applying both types of filters can dramatically improve the signal-to-noise ratio, which is equivalent to ensemble averaging of 130 OAPs. The possibility of using a combination of spatial and temporal filters instead of ensemble averaging is particularly important for optical mapping of wave propagation in the heart during nonstationary cardiac arrhythmias when the latter cannot be applied.

There is a good reason to believe that filter characteristics derived from normal propagation spectra will also be appropriate for processing ventricular fibrillation (VF) data. Indeed, during VF the action potential duration and hence the wavelength shorten significantly (11, 16). However, the highest frequency components related to cardiac propagation in both the spatial and time domains still originate from the excitation front: the steeper the front, the stronger the high-frequency components. It is well known that upstrokes during VF slow down compared with normal propagation (24). Accordingly, a low-pass filter that does not distort the normal fronts will not likely distort fronts during VF. However, the signal-to-noise ratio during VF is in general lower than during normal propagation, and it may be tempting to apply a more aggressive filter; this will likely lead to a more significant distortion of the signal.

The fact that spatial and temporal filters with relatively large kernels do not distort the optical signal may seem to contradict the widespread belief that the upstroke of the cardiac action potential has a duration of ~ 1 ms (6) and that the response of styryl voltage-sensitive dyes used in this study is fast enough to cause any noticeable delay (6, 15, 18). However, this is not the case. Although the fluorescence closely follows the transmembrane potential, the optically recorded action potential acquired from thick myocardial preparations deviates significantly from electrical recordings acquired from microelectrodes (5, 8, 12, 13). It does so because the light acquired by the sensor originates from a deep volume of muscle underlying the detector, and from the neighboring tissue (outside the field of view) that has scattered light captured by the detector (13).

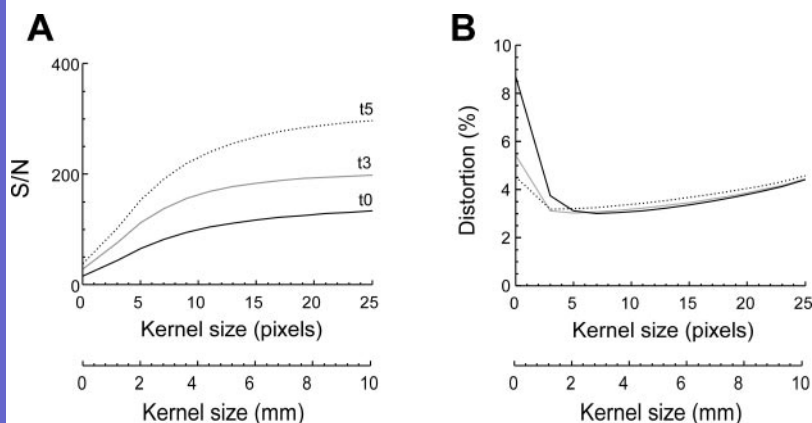


Fig. 8. Effect of combined spatial-temporal filtering on signal-to-noise ratio and distortion. *A*: signal-to-noise ratio is most strongly improved after filtering with a 5-frame temporal kernel (t5; dotted line), but a 3-frame kernel (t3; gray line) also provides significant improvement. *B*: distortion from the combined spatial-temporal filter is lowest for the 5-frame temporal filter with spatial filter kernels smaller than 5×5 pixels (dotted line). For spatial filter kernels larger than 5×5 pixels, a 3-frame temporal filter kernel (gray line) induced almost no distortion relative to no temporal filtering (black line).

This increases the upstroke duration from 1–2 ms to 13 ms or more (12) and results in removing the high frequencies in the spatial domain.

Rational selection of the kernel size. The kernel sizes that we determined were optimized for a particular experimental setup and will change if the pixel size and the frame rate of the recording device are different. However, characteristic spatial scales determined from our spectral analysis of the signal will be preserved, provided the geometry of the tissue and the spectral characteristics of the dye (the wavelength of the excitation and emission light) remain unchanged. This should allow other investigators using thick ventricular preparations to select an appropriate kernel size based on our findings. Assume, for example, we had mapped propagation over a 1.6 cm × 1.6 cm area on the three-dimensional pig ventricular wall using a 16 × 16 photodiode array (1.0 mm/pixel resolution) acquired at 3,000 frames/s (3). According to the criteria derived in this study, the appropriate kernel size for conservative spatial filtering would be 3 × 3 pixels (3.0 × 3.0 mm); a 19-frame kernel would be equivalent to our 5-frame temporal filter. This would result in a 14 × 14 array of filtered signals (signals on the boundary would be unfiltered because of edge effects) with effectively no temporal components above 158 Hz.

Limitations. The slow optical upstroke is a result of the spatial averaging of the signal emitted by the 3-D tissue preparation and is not a property of the optical signal. Therefore, in some preparations where this depth averaging is not present (in 2-D monolayer tissue culture, for example), the optical signal should have a much faster upstroke, and the best spatial filter will have a very small kernel size; this may significantly reduce the effectiveness of spatial filtering. The optimal kernel sizes should also be different in the hearts of small animals such as mice, guinea pigs, and rabbits where the thickness of the wall and thus the degree of blurring of the optical signal is likely to vary. The derivation of the optimal nondistorting filters for these species will require a dedicated study.

Our selection of filter parameters is based on the analysis of filter-induced distortions relative to the EA signal. While the characteristics of the filter are determined by the signal, the effectiveness of the filtering procedure will depend on the signal-to-noise ratio and the degree of spectral overlap between the noise and the signal. When the signal and noise have little spectral overlap (high-frequency noise), one should expect excellent results even at very low signal-to-noise ratios. When the noise spectrum significantly overlaps with the spectral range of the signal, one should not expect good results even with optimal filter parameters.

This analysis concentrated on classical (linear) filtering operations and has demonstrated that spatial filters or combined spatial-temporal filters can significantly improve the signal-to-noise ratio while inducing negligible distortion in movies of optically recorded action potentials. Future studies are needed to evaluate the effectiveness of nonlinear statistical filters, which may produce better movie enhancement with lower distortion (17).

ACKNOWLEDGMENTS

We thank Dr. Peter Swaszek from the Univ. of Rhode Island for helpful comments on the manuscript.

GRANTS

This project was supported in part by National Heart, Lung, and Blood Institute Grants 1RO1-HL-071635–01 and 2PO1-HL-39707 (A. M. Pertsov, S. F. Mironov) and RO1-HL-071762 (A. M. Pertsov) and by National Science Foundation Grant BES-0448050 (F. J. Vetter).

REFERENCES

1. Balboa RM and Grzywacz NM. Power spectra and distribution of contrasts of natural images from different habitats. *Vision Res* 43: 2527–2537, 2003.
2. Chattipakorn N, Banville I, Gray RA, and Ideker RE. Mechanism of ventricular defibrillation for near-defibrillation threshold shocks: a whole-heart optical mapping study in swine. *Circulation* 104: 1313–1319, 2001.
3. Efimov IR and Cheng Y. Optical mapping of cardiac stimulation: fluorescent imaging with a photodiode array. In: *Quantitative Cardiac Electrophysiology*, edited by Cabo C and Rosenbaum DS. New York: Dekker, 2002.
4. Efimov IR, Nikolski VP, and Salama G. Optical imaging of the heart. *Circ Res* 95: 21–33, 2004.
5. Efimov IR, Sidorov V, Cheng Y, and Wollenzier B. Evidence of three-dimensional scroll waves with ribbon-shaped filament as a mechanism of ventricular tachycardia in the isolated rabbit heart. *J Cardiovasc Electrophysiol* 10: 1452–1462, 1999.
6. Fast VG and Kleber AG. Microscopic conduction in cultured strands of neonatal rat heart cells measured with voltage-sensitive dyes. *Circ Res* 73: 914–925, 1993.
7. Field DJ and Brady N. Visual sensitivity, blur and the sources of variability in the amplitude spectra of natural scenes. *Vision Res* 37: 3367–3383, 1997.
8. Gray RA. What exactly are optically recorded “action potentials”? *J Cardiovasc Electrophysiol* 10: 1463–1466, 1999.
9. Gray RA, Jalife J, Panfilov A, Baxter WT, Cabo C, Davidenko JM, and Pertsov AM. Nonstationary vortexlike reentrant activity as a mechanism of polymorphic ventricular tachycardia in the isolated rabbit heart. *Circulation* 91: 2454–2469, 1995.
10. Huang AH, Sofola IO, Bufkin BL, Mellitt RJ, and Guyton RA. Coronary sinus pressure and arterial venting do not affect retrograde cardioplegia distribution. *Ann Thorac Surg* 58: 1499–1504, 1994.
11. Huang J, Zhou X, Smith WM, and Ideker RE. Restitution properties during ventricular fibrillation in the in situ swine heart. *Circulation* 110: 3161–3167, 2004.
12. Hyatt CJ, Mironov SF, Vetter FJ, Zemlin CW, and Pertsov AM. Optical action potential upstroke morphology reveals near-surface transmural propagation direction. *Circ Res* 97: 277–284, 2005.
13. Hyatt CJ, Mironov SF, Wellner M, Berenfeld O, Popp AK, Weitz DA, Jalife J, and Pertsov AM. Synthesis of voltage-sensitive fluorescence signals from three-dimensional myocardial activation patterns. *Biophys J* 85: 2673–2683, 2003.
14. Lin SF, Roth BJ, and Wikswo JP Jr. Quatrefoil reentry in myocardium: an optical imaging study of the induction mechanism. *J Cardiovasc Electrophysiol* 10: 574–586, 1999.
15. Loew LM, Cohen LB, Dix J, Fluhrer EN, Montana V, Salama G, and Wu JY. A naphthyl analog of the aminostyryl pyridinium class of potentiometric membrane dyes shows consistent sensitivity in a variety of tissue, cell, and model membrane preparations. *J Membr Biol* 130: 1–10, 1992.
16. Omichi C, Zhou S, Lee MH, Naik A, Chang CM, Garfinkel A, Weiss JN, Lin SF, Karagueuzian HS, and Chen PS. Effects of amiodarone on wave front dynamics during ventricular fibrillation in isolated swine right ventricle. *Am J Physiol Heart Circ Physiol* 282: H1063–H1070, 2002.
17. Pratt WK. *Digital Image Processing*. New York: Wiley, 1978.
18. Salama G. Optical measurement of transmembrane potential in heart. In: *Probes of Membrane Potential*, edited by Loew L. Boca Raton, FL: Uniscience, 1988, p. 137–199.
19. Seul M, O’Gorman L, and Sammon MJ. *Practical Algorithms for Image Analysis*. Cambridge, UK: Cambridge Univ. Press, 2000.
20. Skanes AC, Mandapati R, Berenfeld O, Davidenko JM, and Jalife J. Spatiotemporal periodicity during atrial fibrillation in the isolated sheep heart. *Circulation* 98: 1236–1248, 1998. [Comment in: *Circulation* 100: 212, 1999.]

21. **Sung D, Cosman JSJP, Mills R, and McCulloch AD.** Phase shifting prior to spatial filtering enhances optical recordings of cardiac action potential propagation. *Ann Biomed Eng* 29: 854–861, 2001.
22. **Witkowski FX, Leon LJ, Clark ML, Ditto WL, and Giles WR.** A method for visualization of ventricular fibrillation: design of a cooled fiber optically coupled image intensified CCD data acquisition system incorporating wavelet shrinkage based adaptive filtering. *Chaos* 8: 94–102, 1998.
23. **Zaitsev AV, Berenfeld O, Mironov SF, Jalife J, and Pertsov AM.** Distribution of excitation frequencies on the epicardial and endocardial surfaces of fibrillating ventricular wall of the sheep heart. *Circ Res* 86: 408–417, 2000.
24. **Zhou X, Guse P, Wolf PD, Rollins DL, Smith WM, and Ideker RE.** Existence of both fast and slow channel activity during the early stages of ventricular fibrillation. *Circ Res* 70: 773–786, 1992.

